POSEIDON WATER

Appendix F
Water Circulation in Agua Hedionda Lagoon

Renewal of NPDES CA0109223
Carlsbad Desalination Project

Biological Considerations of Water Circulation in Agua Hedionda Lagoon Under Long Term Stand-Alone Operations of the Carlsbad Desalination Project

Submitted by:
Scott A. Jenkins, Ph. D.
Dr. Scott A. Jenkins Consulting
14765 Kalapana Street, Poway, CA 92064

Submitted to:
Poseidon Water LLC
5780 Fleet Street, Suite 140
Carlsbad, CA 92008

4 Spetember 2015

1) Abstract:

This technical note details tidal hydraulic simulations of the flow field in Agua Hedionda Lagoon for the tidal conditions and water withdrawal anticipated for the stand-alone Carlsbad Desalination Project. These simulations allow us to map out the water circulation throughout the lagoon with special attention placed on the West Basin and the tidal inlet channel. These simulations reveal a quiescent area in the southeast corner of the West Basin of the lagoon where fish can be returned to the lagoon after recovery by up-graded fish screens without significant risk for recirculation of returned organisms into the intake flow.

2) Technical Approach:

Spring, neap and mean tidal range simulations of the hydraulics of Agua Hedionda Lagoon were performed using astronomic tidal forcing functions at = 2 sec time step intervals for the period 1980-2007. Computed water surface elevations and depth averaged velocities from the global solution matrix were converted to lagoon waterline contours and flow trajectories. Calibrations for determining the appropriate Manning factors and eddy viscosities were performed by running the TIDE_FEM model on the Figure 1 bathymetry file and comparing calculated water surface elevations in the East Basin and inlet channel velocities against measurements by Elwany et al. (2005) during a complete spring-neap cycle of 13 -30 June 2005. Plant flow rates during this lagoon monitoring period were input to TIDE_FEM (APPENDIX-I) according to daily recordings by Cabrillo LLC. Iterative selection of Manning factor n_0 = 0.03011 and an eddy viscosity of ε = 6.929 ft^2/sec gave calculations of water surface elevation

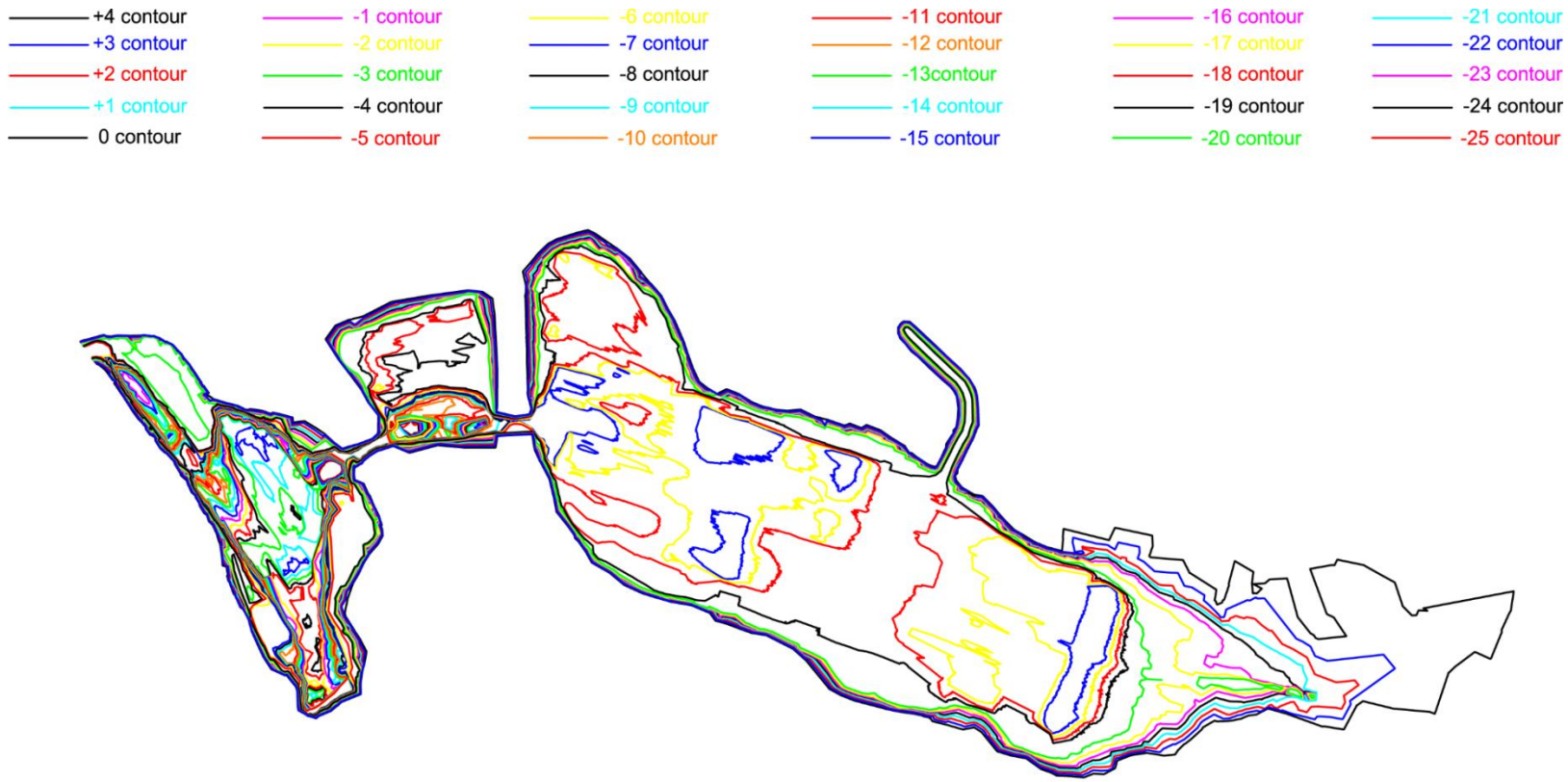

Figure 1 . Agua Hedionda bathymetry in ft NGVD, based on 2007 survey for -2 ft thru -25 ft; and on 1997 survey for +4 thru -2 ft.

and inlet channel velocities that reproduced the measured values to within 2% over the 18 day spring-neap monitoring cycle.

Figure 2 gives the flow trajectories and depth averaged tidal currents computed by the calibrated TIDE_FEM model during spring flooding tides on 21 June 2005 of the monitoring period from Elwany et al (2005). The model was initialized with a plant flow rate of 501.1 mgd as reported by Cabrillo Power LLC. This flow rate is roughly equivalent to the long-term mean. Maximum currents in the inlet channel reached 1.5 m/sec or 4.9 ft/sec. Flood tide currents in the West Basin form a well-defined jet along the north bank at speeds of between 0.9 m/s (2.9 ft/sec) to 1.2 m/sec (3.9 ft/sec), sufficient to scour and transport fine sand in the 120-210 micron size regime. A sluggish eddy persists in the central portion of the West Basin while the middle portion of the recharge zone is near stagnation, ideal conditions for fine sand to settle in deep water post dredging bathymetry. A feeder current of about -0.4 m/sec (-1.3 ft/sec) spins off the southeast flank of the West Basin eddy, and flows toward the plant intake, thereby supplying feed water at a rate of 501 mgd to the plant. The flood tide jet along the north bank of the West Basin speeds back up to as high as 1.5 m/sec (4.9 ft/sec) as it passes through the hardened channel under the rail road bridge and then losses energy as it diverges into the Central Basin, spinning up a somewhat disorganized Central Basin eddy. The core of the Central Basin eddy is at stagnation, again providing ideal conditions for suspended sediment to settle and deposit. Consequently a bar forms here that was removed during the 1997-98 inner basin restoration dredging performed by SDG&E (Jenkins and Wasyl, 1998). Spring flood tide currents speed back up to 0.8-0.9 m/sec (2.6-2.9 ft/sec) through the hardened channel under the I-5 bridge before diverging into a complex set of counter rotating eddies that populate the East Basin. East Basin eddy speeds are on the order of 0.1 m/sec (0.3 ft/sec), insufficient to transport fine sand but an important stirring mechanism for mixing the East Basin water mass to maintain high oxygen levels and to maintain silt and clay sized sediment particles in suspension.

Figure 3 plots the TIDE_FEM simulation of ebbing spring tidal flows in the lagoon on 21 June 2005. The wetted area of the lagoon is significantly reduced relative to the flood tide area in Figure 2, due to the lower water levels acting on the storage rating curve. A creeping flow with complex structure on the order of -0.1 m/sec (-0.3 ft/sec) evacuates the east basin and accelerates to -0.8 m/sec (-2.6 ft/sec) as it passes through the hardened channel under the I-5 bridge. A vigorous well-ordered Central Basin eddy is spun up by an ebb-tide jet flowing along the southern bank of the Central Basin. This jet accelerates to -2m/sec (-6.6 ft/sec) as it passes through the hardened channel under the rail road bridge; and then splits into a south branch current and a north branch current as it diverges into the West Basin. The south branch current flows along the west bank of the West Basin and feeds the power plant source water at a rate of about -0.6 m/sec (-2.0 ft/sec). The north branch current also flows along the west bank of the West Basin and exits the lagoon through the ocean inlet. Maximum ebb flow currents in the inlet channel are only -0.8 m/sec (2.6 ft/sec) as the ebb flow volume flux is divided between the power plant intake and the ocean inlet. This is sufficient to flush the finer grain sizes from the bar in the recharge zone but not the coarser fractions in the 200 micron range. Thus the ebb tide flux that is scavenged by the power plant seawater consumption reduces the lagoons ability to flush sand from the lagoon even during spring tides.

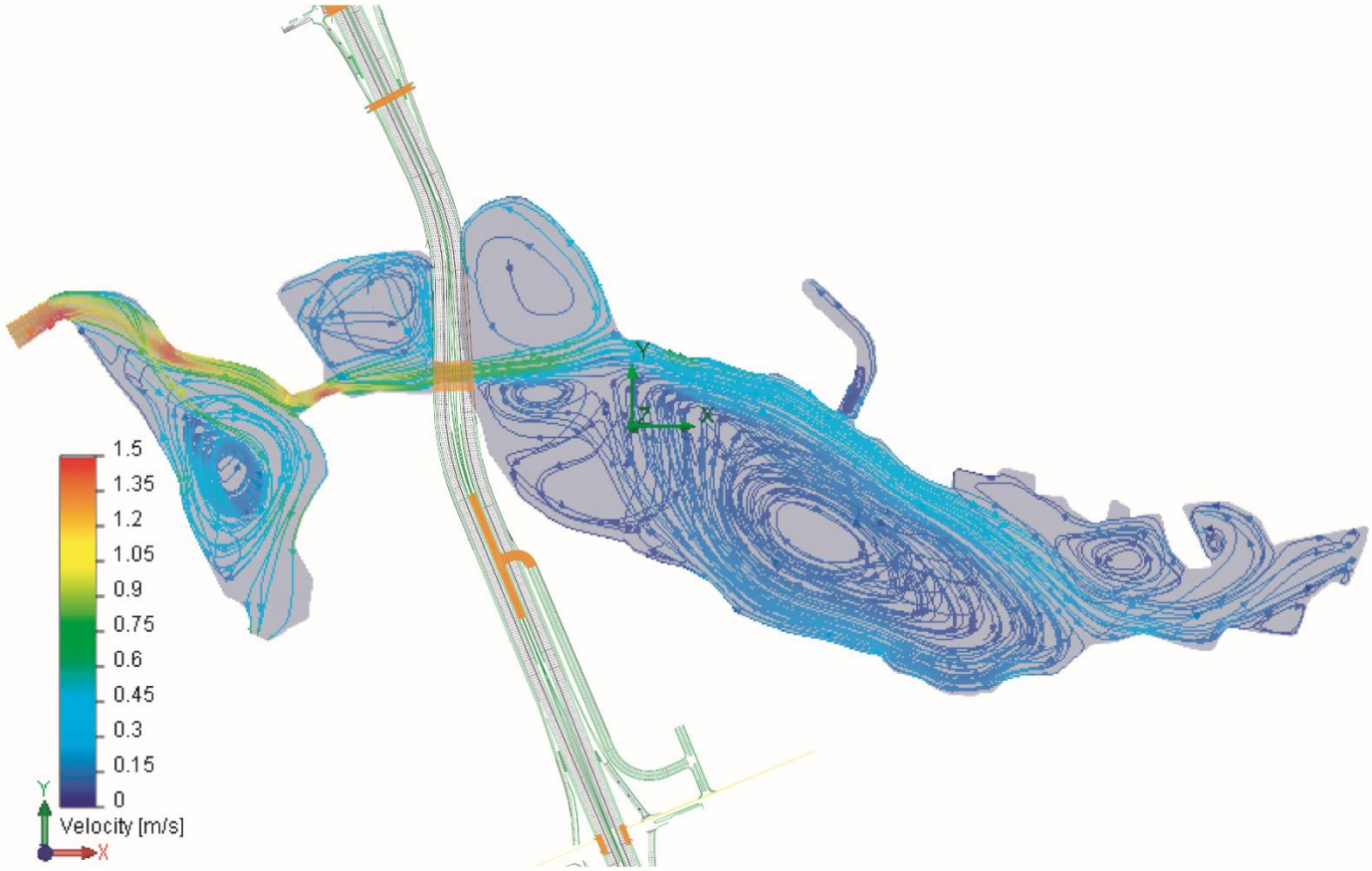

Figure 2. Hydrodynamic simulation of tidal flow into Agua Hedionda Lagoon during spring flooding tides.

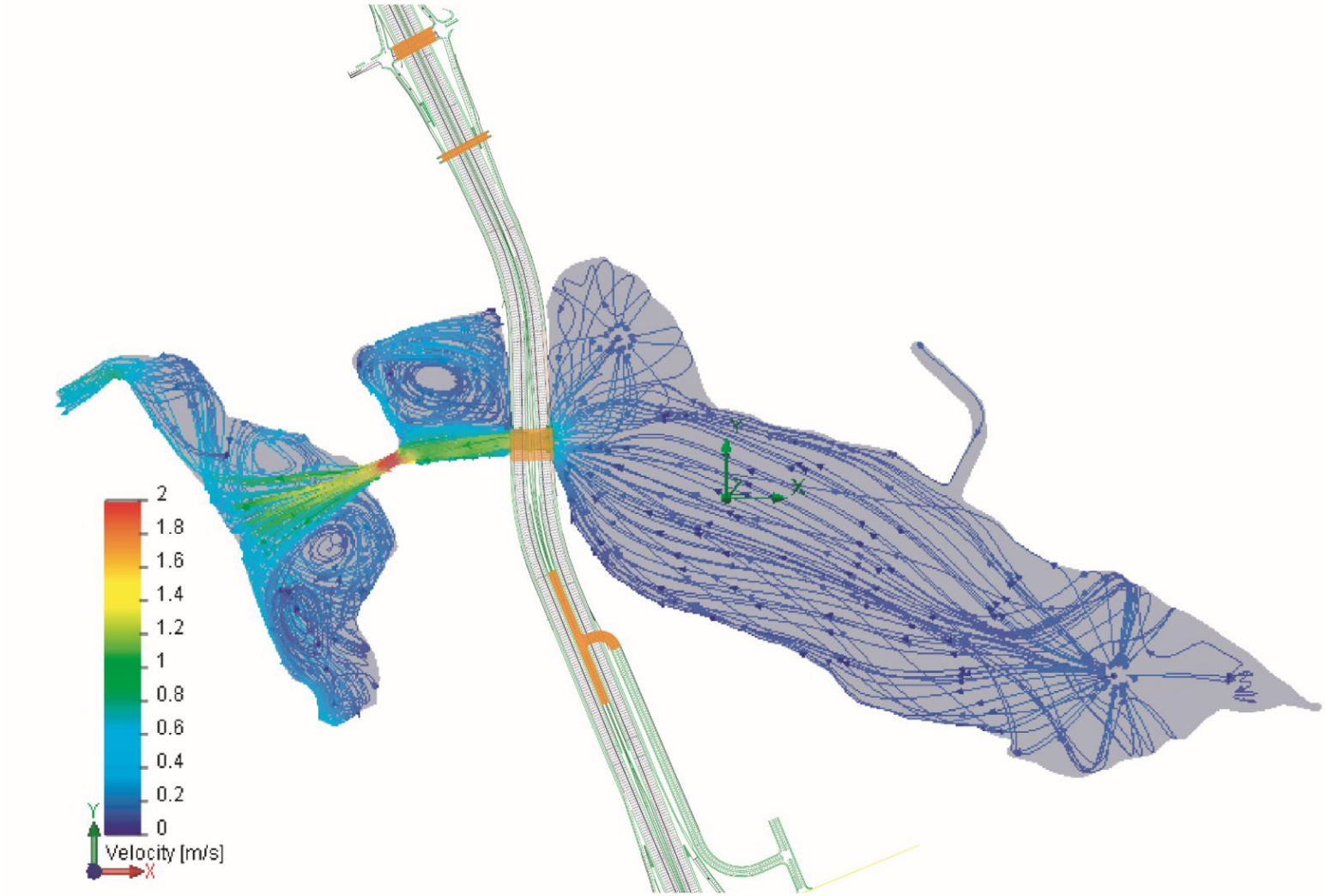

Figure 3. Hydrodynamic simulation of tidal flow out of Agua Hedionda Lagoon during spring ebbing tides.

Hydrodynamic simulations of flooding and ebbing neap tide currents on 14 June 2005 are plotted in Figures 4 & 5, respectively. The plant flow rate on this date remained at 501.1 mgd. The neap tide simulations show very similar flow structures as the spring tide simulations in Figures 2 & 3, only more sluggish and with less contrast in wetted lagoon area between flood and ebb due to the small tidal range during neap tides. Eddy systems remain well organized in the East Basin during flooding neap tides (Figure 4) and a weak boundary current (0.2 m/sec or 0.6 m/sec) flows along the north bank, helping to stir the East Basin water mass in spite of the relatively low energy of the system. Maximum inlet channel currents reach 0.7 m/sec (2.3 ft/sec) during flooding neap tides (Figure 4), less than half the inlet channel speeds as occurred during flooding spring tides at equivalent plant flow rate in Figure 2. Maximum inlet channel currents during ebbing neap tide (Figure 5) drop to only -0.2 m/sec (-0.7 ft/sec), well below the threshold of motion of the 120-210 micron fine sand on the West Basin bar in the recharge zone. Those no sand is flushed from the lagoon during neap tides.

TIDE_FEM simulations of flooding and ebbing currents during mean tidal ranges on 30 June 2005 are plotted in Figures 6 & 7, respectively. The plant flow rate on this date was very low, reduced to 207.4 mgd, well below the long term mean or even the flow requirements for the Carlsbad Desalination Project. Again, the mean tide simulations show similar flow structures as the spring tide simulations in Figures 2 & 3, and although a bit more sluggish the wetted lagoon areas during flood and ebb and ebb are somewhat comparable to the spring tide cases. The south branch ebb current in the West Basin is significantly diminished due to the low plant flow rate, reaching only -0.2 m/sec (-0.6 ft/sec). The significant distinction of these mean tide simulations in Figures 6 & 7 is how the reduced plant flow rate has muted the flood flow currents in the inlet channel and allowed the ebb flow currents to be nearly comparable to spring tides and above threshold speed for the finer grain size fractions on the bar in the recharge zone. Maximum flood flow currents in the inlet channel during mean tides (Figure 6) reach 1.0 m/sec (3.2 m/sec), while maximum ebbing currents in the inlet during mean tides (Figure 7) remain at -0.6 m/sec (2.0 ft/sec), sufficient to scour and flush 120-180 micron size sand fractions from the bar in the recharge zone. Thus, reduction in plant flow rates affords improved flushing of sand from the lagoon during ebb tide, even at average tidal ranges.

3**) Model Validation and Error Analysis:**

Figure 8 provides a quantitative assessment of the accuracy of the calibrated TIDE_FEM model over the entire 18 day calibration period of 13-30 June 2005. Here we compare East Basin water level variations predicted by the model (purple trace) with the actual water level measurements (black crosses) by Elwany et. al., (2005). The East Basin water level variations in purple are found to lag the ocean water levels by as much as 47 minutes during the spring tides on 21 June 2005, and this phase lag averages 39 minutes over the entire 18 day spring-neap cycle. The amplitudes and degree of non-linearity in the East Basin water level time series simulated by the model closely duplicate that observed in the measured lagoon tides. The maximum error in simulating the low tide elevations was found to be ε_L = +0.1 ft. The

maximum high tide error in the model simulation relative to observations was found to be ε_H = -0.05 ft. Consequently, the calibration error appears to exhibit a systematic tendency. When amplitude errors occur they tend to over estimate the water elevation of the LLW tidal stage, and under estimate the water elevation of the HHW tidal stage. Although these errors are quite small and may be considered high predictive skill, this error mode would be consistent with

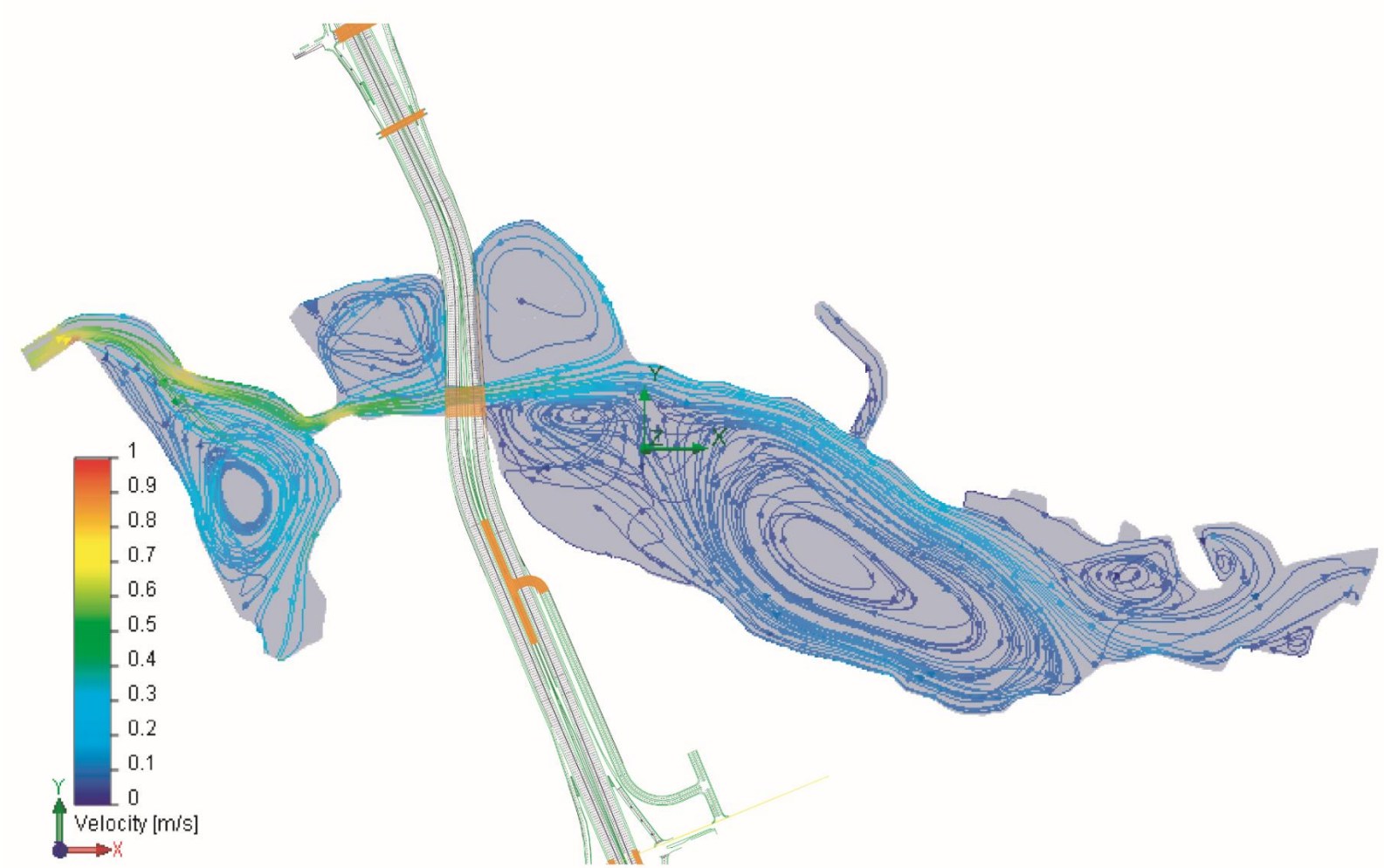

Figure 4. Hydrodynamic simulation of tidal flow into Agua Hedionda Lagoon during neap flooding tides.

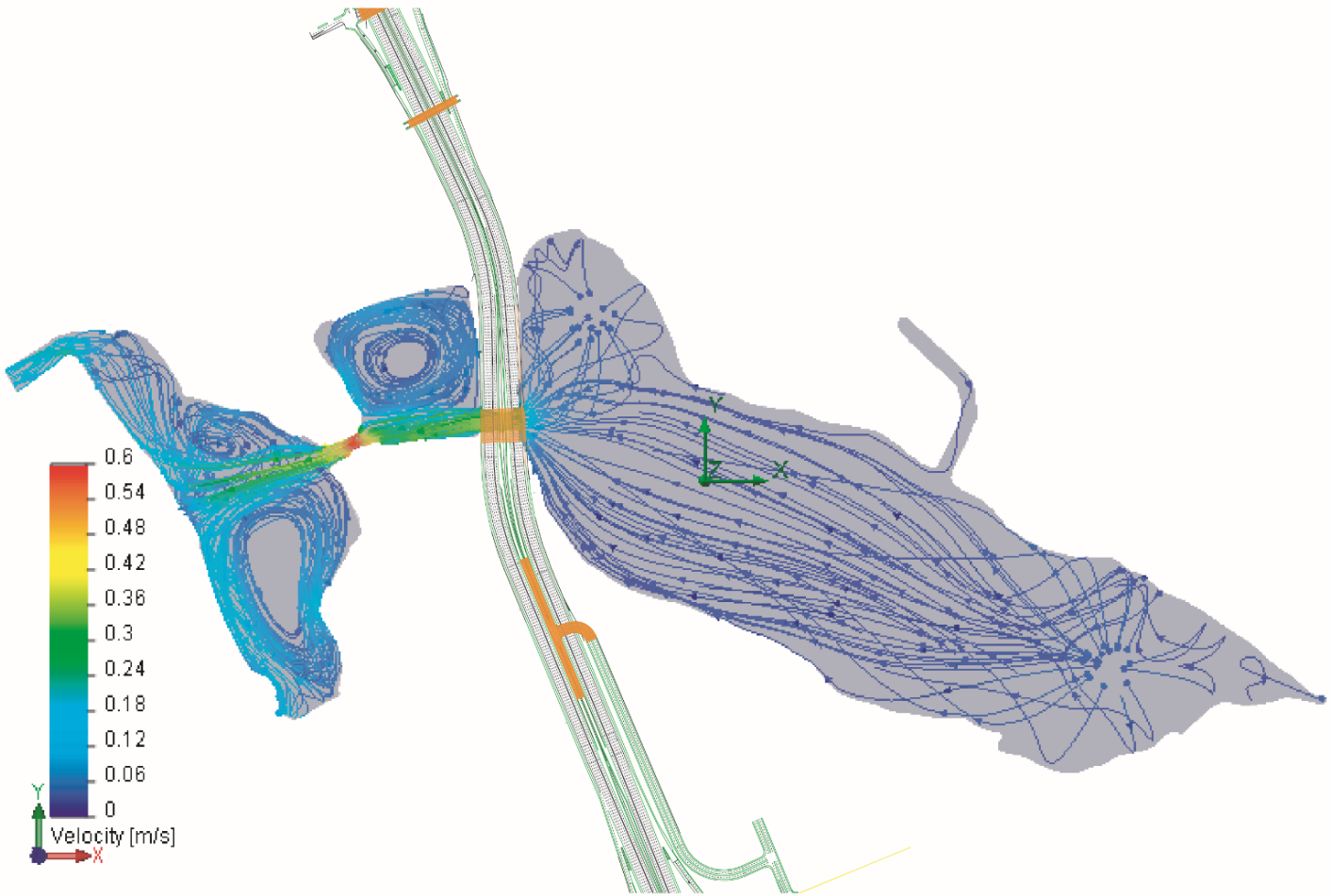

Figure 5. Hydrodynamic simulation of tidal flow out of Agua Hedionda Lagoon during neap ebbing tides.

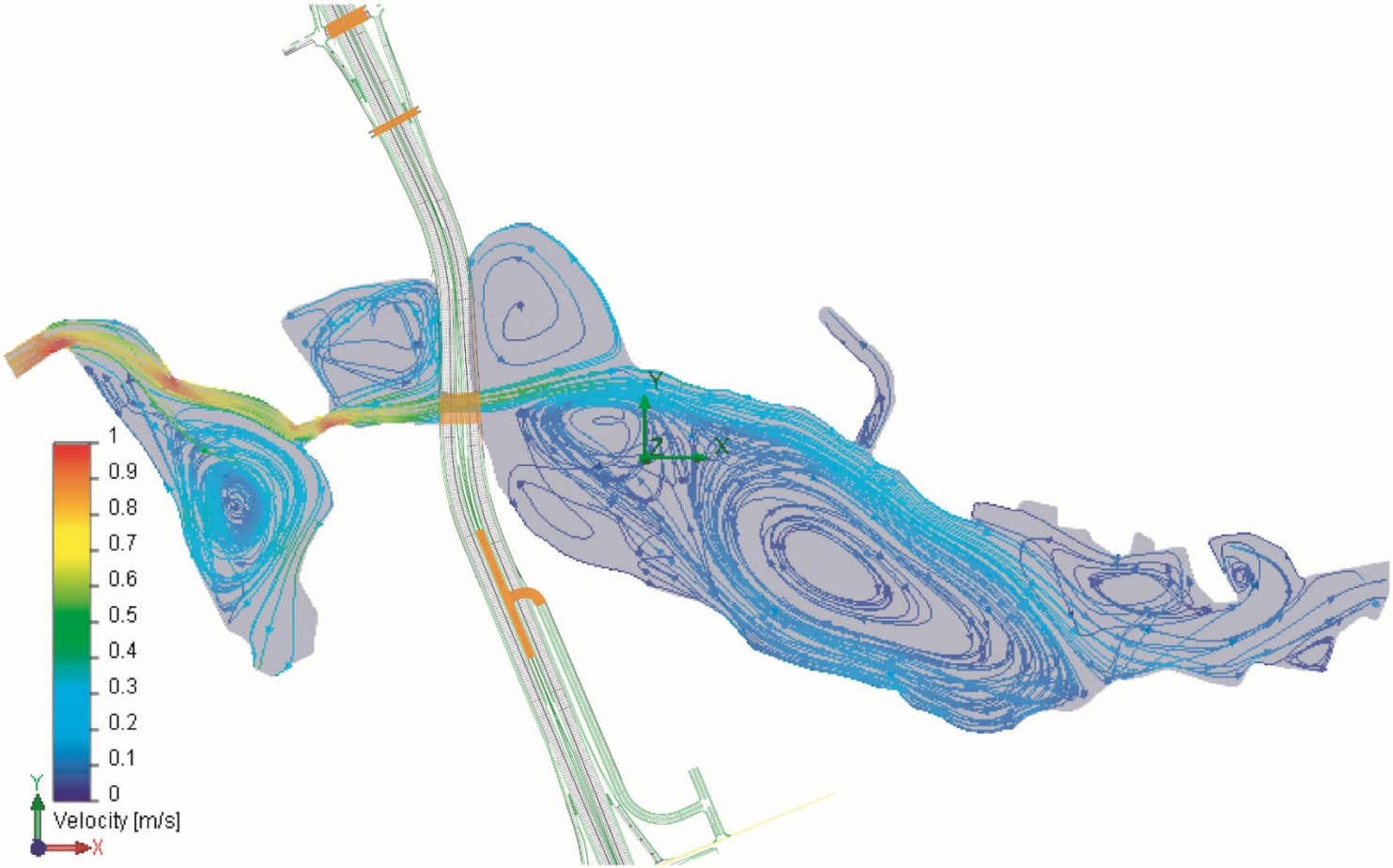

Figure 6. Hydrodynamic simulation of tidal flow into Agua Hedionda Lagoon during mean flooding tides.

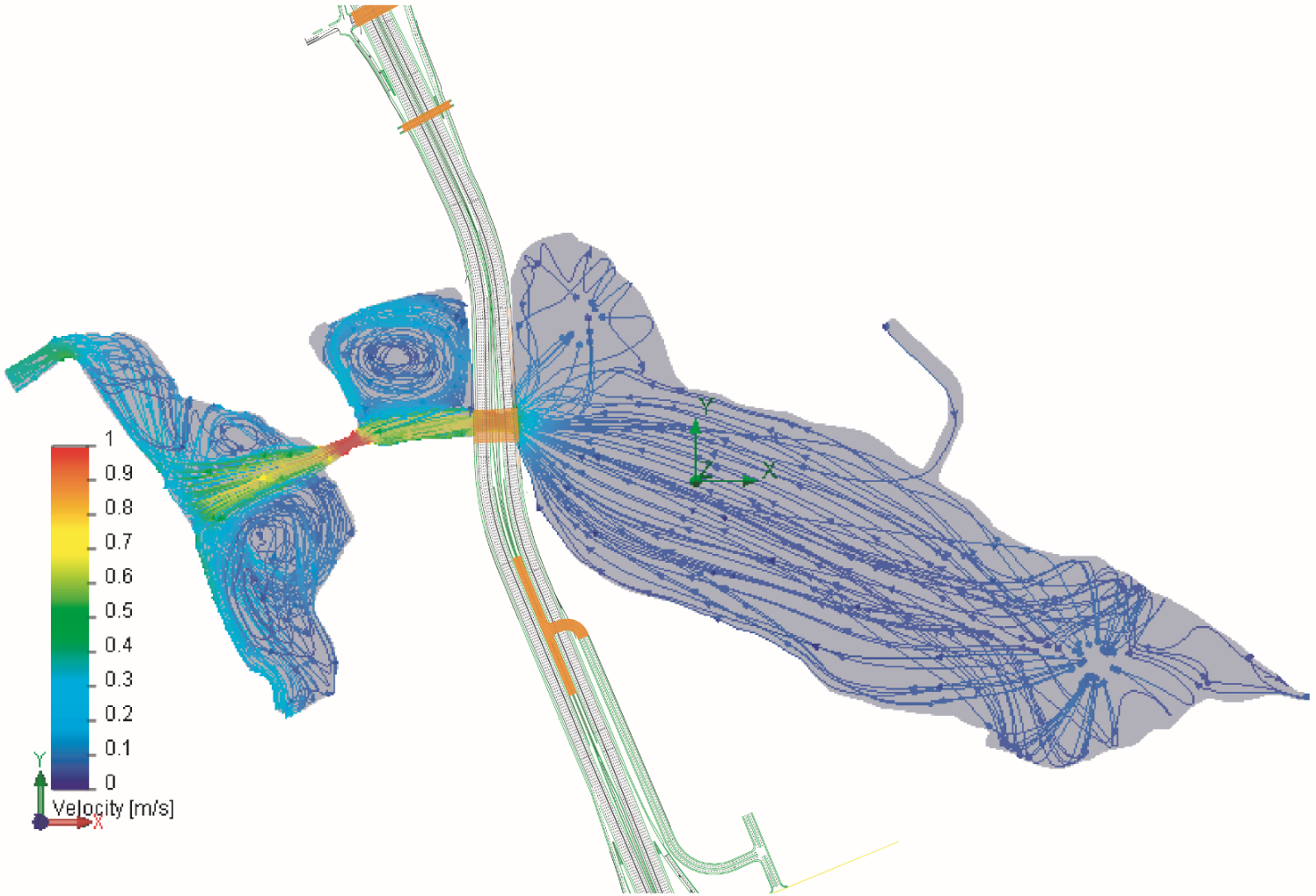

Figure 7. Hydrodynamic simulation of tidal flow out of Agua Hedionda Lagoon during mean ebbing tides.

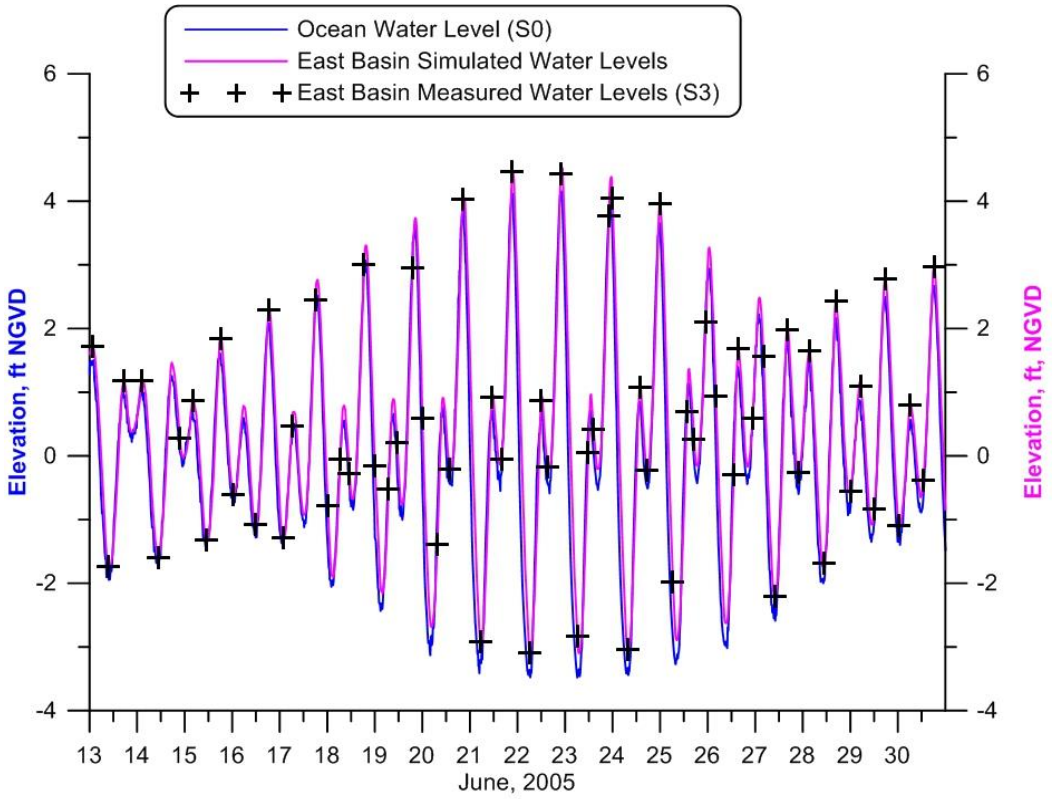

Figure 8: TIDE_FEM model calibration using spring-neap cycle water level measurements from Elwany, et al. 2005. Ocean water levels (S0) indicated in blue; hydrodynamic simulation of east basin water levels shown in purple, east basin water level measurements (S3) shown as black crosses.

bathymetry errors in which depth has been under estimated, Weiyan (1992). Bathymetry errors are the most common cause of modeling errors. Other sources of errors include:

ELEMENT INTERPOLATION ERROR: Due to the degree of the polynomial used to specify shape function, N_i.

DISCRETIZATION ERRORS: Due to mesh coarseness and approximating the curved wet/dry boundary side of an element with a quadratic spline.

QUADRATURE ERRORS: Due to reducing the weighted residual integrals with the influence coefficient matrices.

ITERATION ERRORS: Due to solving the system of algebraic equations reduced from the Galerkin Equations.

ROUNDOFF ERRORS: Due to time integration by the trapezoidal rule.

SEA LEVEL ANOMALIES: Due to discrepancies between the astronomic tides and the actual observed water levels in the ocean.

INSUFFICIENT CALIBRATION DATA: Due to limitations in the period of record.

Power (auto-) spectra are useful tools for determining how the energy in complex time series like Figures 8 is distributed among various frequencies of oscillation. The predominant frequencies where most of the current energy appears (spectral peaks) can give clues that identify the mechanisms that predominate in the local tidal system. In Figure 9, auto spectra of the ocean tides (blue, upper panel) shows the predominant energy is centered on a diurnal frequency 10^{-5} Hz of the K1 lunar-solar diurnal tidal constituent at $f_{K1} = 1.16079 \text{ x } 10^{-5}$ Hz. The energy in this peak is disproportionately high relative to the next largest spectral peak occurring at the M2 principal lunar semi-diurnal tidal constituent, $f_{M2} = 2.2365 \text{ x } 10^{-5}$ Hz. The excess energy at diurnal frequencies is believed to be non-tidal and attributable to a wind-driven current component that has a diurnal fluctuation in response to daily heating of the land. With the onset of summer heating of the inland deserts, this diurnal sea breeze component would be strengthening in the June time frame of the 2005 lagoon monitoring.

Other less energetic tidal peaks are also found in the spectra of Figure 9 including one believed to be a baroclinic *shelf resonance* formed by a resonant *triad* at the sum of the frequencies of the K1 and M2 barotropic tides, ie a diurnal third harmonic at a frequency $f_3 = f_{K1} + f_{M2} = 3.3973 \text{ x } 10^{-5}$ Hz. This diurnal third harmonic is a baroclinic tide excited by the barotropic K1 and M2 tides interacting with the bottom topography, in particular the Carlsbad Submarine Canyon. Another baroclinic shelf resonance apparent in the spectra of the ocean tides in Figure 9 is a second harmonic of the barotropic M2 tide appearing at a frequency of $2 f_{M2} =$ $4.4730 \text{ x } 10^{-5}$ Hz. The auto spectra of the east basin tides shown in green in the lower panel of Figure 9 exhibits the same primary barotropic and baroclinic tidal peaks as the ocean tides in the upper panel; with one exception; an additional non-linear resonance appears as a triad formed by the sum of the K1 barotropic mode and the baroclinic second harmonic of the M2 tide, $f_{K1} + 2 f_{M2} = 5.6338 \text{ x } 10^{-5}$ Hz. Apparently this mode is excited by non-linear tidal interaction with the lagoon bathymetry.

The other quantitative data used to assess the accuracy of the calibrated TIDE_FEM model are the inlet channel currents, measured by Elwany et. al., (2005) during the lagoon

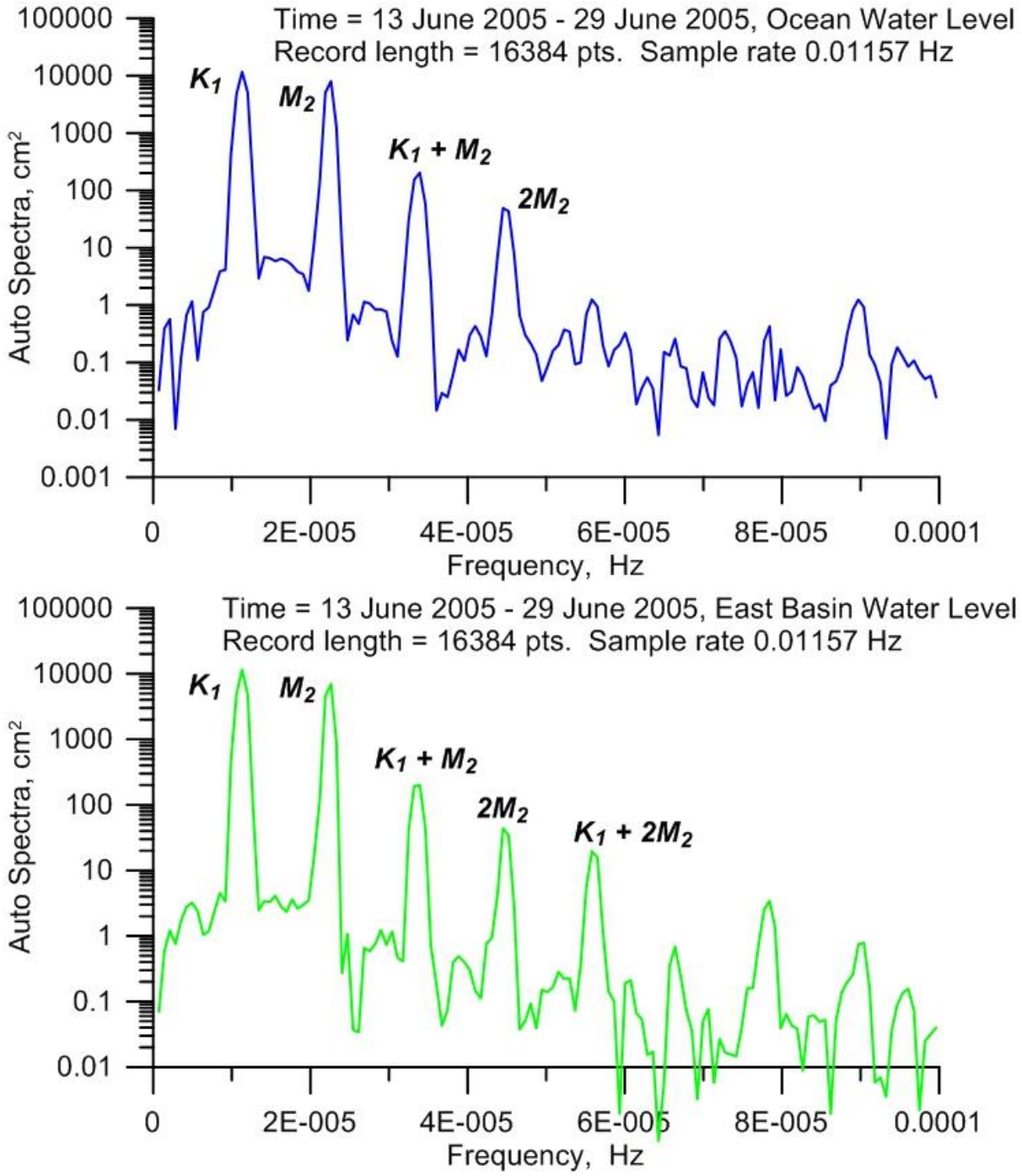

Figure 9 . a) Ocean water level spectra; b) Agua Hedionda East Basin water level spectra, 13 - 29 June 2005.

monitoring period of 13-30 June 2005. Figure 10 compares the TIDE_FEM model simulations of inlet channel currents (green) against inlet velocity measurements (black crosses). For reference, the ocean tides are indicated in blue. The flood and ebb current maximums and minimums in the inlet channel are found to lead the high and low ocean water levels by as much as 13.7 hours during the spring tides on 21 June 2005. Maximum flood tide currents on this day were 5.16 ft/sec, while maximum ebb tide currents were -2.87 ft/sec; the flood tide dominance due to the scavenging effect of the power plant intake rate on the available lagoon water volume which was operating at 501 mgd. Throughout the 18 day monitoring period, average flood tide currents in the inlet channel were 1.91 ft/sec while average ebb tide currents were -0.91 ft/sec while the power plant averaged an intake flow rate of 430.97 mgd. The amplitudes and degree of non-linearity in the inlet current time series simulated by the model closely duplicate that observed in the measured currents. The maximum error in simulating the ebb tide currents was found to be ε_L = +0.1 ft/sec. The maximum flood tide error in the modeled currents relative to observations was found to be ε_H = -0.05 ft/sec. Again, this type of systematic simulation error is characteristic of bathymetry errors in the model input file; however, the size of these errors is well within what is considered to be high predictive skill.

Figure 11 compares the auto spectra of the inlet channel currents in green in the lower panel against the ocean tidal spectra from Figure 9 in blue in the upper panel. Spectral peaks in the ocean tides are all found in the spectra of the inlet channel currents but some of the higher harmonics are disproportionately large and there are also additional higher harmonics not found in the ocean tides. In particular, the M2 tidal peak in the spectra of the inlet channel currents has more energy than the K1 peak. This is probably indicative of non-linear friction effects on the inlet channel currents, producing a second harmonic of the diurnal K1 component that overlays on the semidiurnal M2. The diurnal third harmonic is present in the inlet channel currents at the sum of the frequencies of the K1 and M2 barotropic tides, as well as the second harmonic of the M2 tides. But we also find in the inlet channel current spectra the triad observed in the east basin water level spectra (Figure 9) formed by the sum of the K1 barotropic mode and the baroclinic second harmonic of the M2 tide; so apparently that non-linear bathymetric mode was excited at the inlet. Further evidence of non-linear friction interacting with bathymetry is the presence of additional triads at higher harmonics of the inlet channel current spectra. These harmonics are not present with significant energy in the East Basin water level spectra of Figure 9. These frictionally generated harmonics include a second harmonic of the triad formed by the sum of the K1 barotropic mode and the baroclinic second harmonic of the M2 tide, $2\,(f_{K1} + f_{M2}) =$

6.7946×10^{-5} Hz; and a triad formed by the sum of the K1 barotropic mode and the baroclinic third harmonic of the M2 tide, $f_{K1} + 3f_{M2} = 7.8703 \times 10^{-5}$ Hz. The presence of these non-linear higher harmonics in the inlet channel currents exert a strong influence on the transport of sand into the West Basin, as sediment transport is proportional to the cube of the inlet channel velocity.

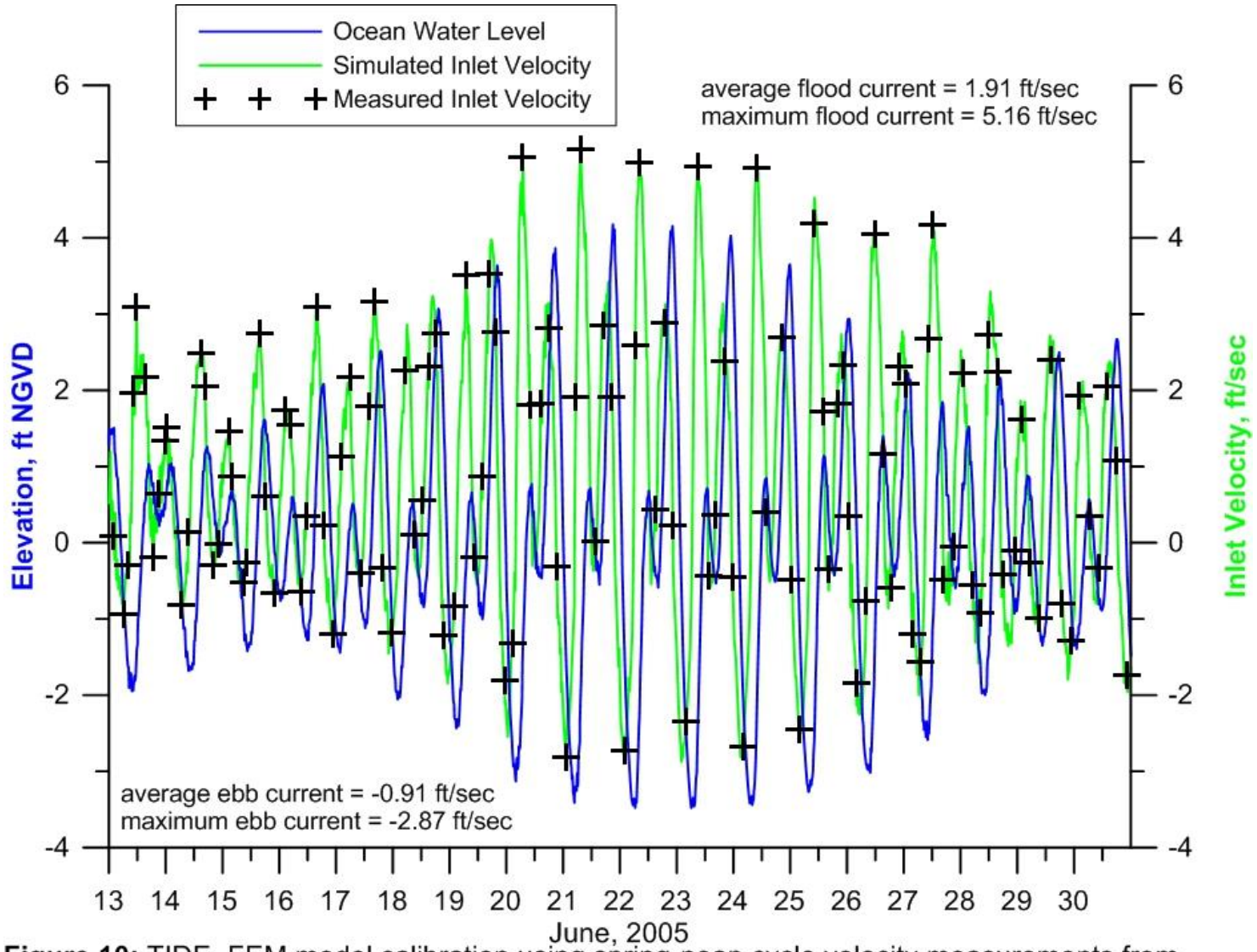

Figure 10: TIDE_FEM model calibration using spring-neap cycle velocity measurements from Elwany, et al. 2005. Ocean water levels (S0) indicated in blue; hydrodynamic simulation of inlet velocity shown in green, inlet velocity measurements (S0) shown as black crosses.

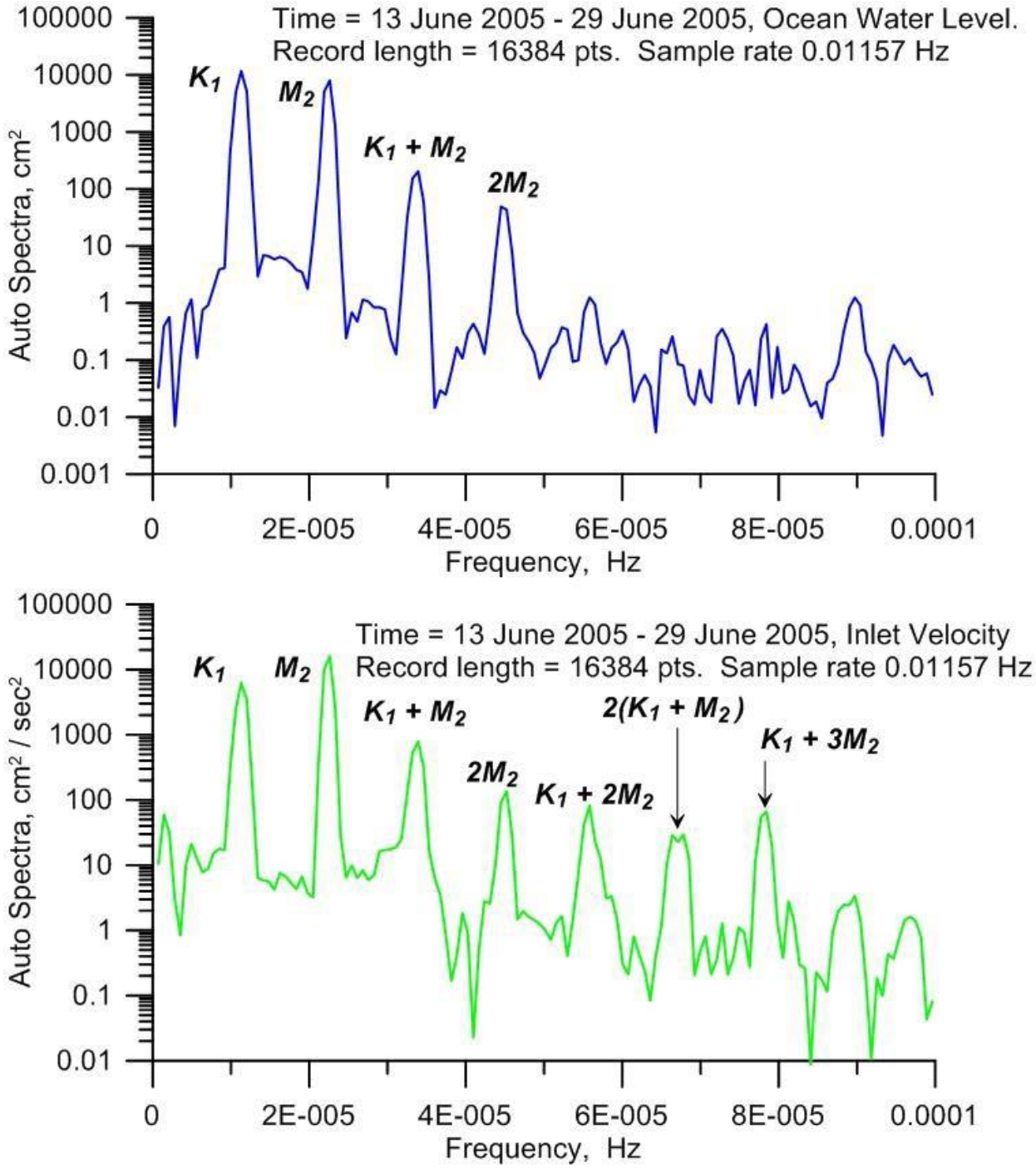

Figure 11 . a) Ocean water level spectra; b) Agua Hedionda inlet velocity spectra, 13 - 29 June 2005.

As a final test of the calibration and stability of the TIDE_FEM model we perform an ultimate simulation of the tidal transport in Agua Hedionda during the highest ocean water level ever recorded. This is referred to as the extreme high water (EHW) level and occurred during the 1997 El Nino on 13 November 1997 when ocean water levels reached 7.65 ft MLLW at the Scripps Pier tide gage. (One of the utilities of hydrodynamic models is in the recreation of extreme events that were not well observed). Figure 12 shows the flood flow simulation of Agua Hedionda Lagoon during the 13 November 1997 extreme high water level event. It displays many similar flow structures to the spring tide flood flow simulation in Figure 2, although the wetted footprint of the lagoon is significantly larger and more complex during the EHW event. To facilitate comparisons with Figure 2, the EHW simulation in Figure 12 is based on an equivalent plant flow rate of 501.1 mgd, or about the same as the long term mean. Figure 12 reveals maximum currents in the inlet channel reach 2.2 m/sec or 7.2 ft/sec. The flood tide jet along the north bank of the West Basin sustains speeds of between 1.5 m/s (4.9 ft/sec) to 2.0 m/sec (6.5 ft/sec), well above the threshold of motion of the fine sand on the bar in the recharge zone and more than sufficient to induce scour and erosion of those sands. The eddy in the central portion of the west basin spins at 0.4 m/sec (1.3 ft/sec) but the middle portion of the recharge zone remains near stagnation. The feeder current toward the plant intake runs at about -0.4 m/sec (-1.3 ft/sec), the same as in the spring tide simulation in Figure 2 since both simulations are using the same plant flow rate, and circulation in the southern end of the West Basin is largely driven by plant flow rate. The flood tide jet along the north bank of the West Basin speeds back up to as high as 1.8 m/sec (5.9 ft/sec) as it passes through the hardened channel under the rail road bridge and then spins up a somewhat more orderly Central Basin eddy. The core of the Central Basin eddy remains at stagnation, again providing ideal conditions for suspended sediment to settle and deposit. Flood tide currents during the EHW event speed back up to 1.0 m/sec (3.2 ft/sec) through the hardened channel under the I-5 bridge before diverging into a complex set of rather vigorous counter rotating eddies that populate the East Basin. This eddy structure includes 5 counter rotating eddies in the East Basin, two more than found for the spring tide flood simulation in Figure 2. East Basin eddy speeds are on the order of at 0.4 m/sec (1.3 ft/sec), for times stronger than for the spring tide flood simulation in Figure 2. The high marsh area at the east end of the East Basin exhibits a disorganized meandering flow system during the EHW event. From this collection of calibration scenarios, we conclude that the TIDE_FEM model remains stable and well-behaved for all the most extreme possible water level variations.

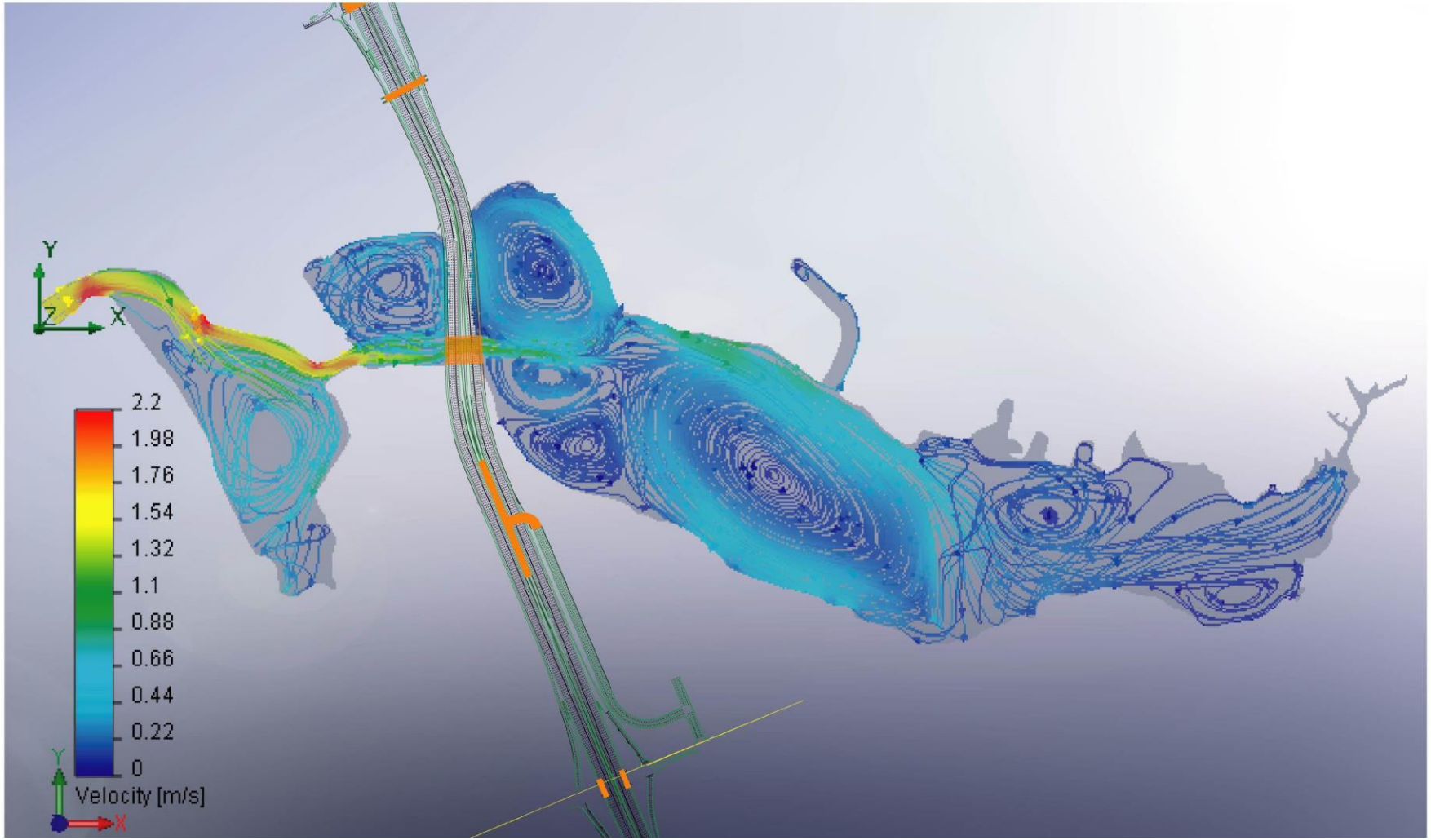

Figure 12: Hydrodynamic simulation of tidal flow into Agua Hedionda Lagoon during extreme high-water flooding tides

4) Intake Flow Rate under Long Term Standalone Operation:

The forthcoming completion of the 50 mgd Carlsbad Desalination Project will set a limit on daily consumption of Agua Hedionda Lagoon water at 304 mgd, as this is the minimum flow required to produce 50 mgd of product water while maintaining sufficient initial in-the-pipe dilution of 50 mgd of brine to be discharged into near shore waters on the open coast..

5) Velocity and Shear Stress Distribution in the West Basin of the Lagoon:

With background on Encina intake flow rate history, we consider the variability in the velocity and shear stress field of the West Basin of Agua Hedionda Lagoon and the entrance to the Encina seawater circulation system. Figure 13 provides a contour map of the velocity field in the West Basin of Agua Hedionda Lagoon at maximum flood tide flow during spring tide with intake flow rate, Q = 304 mgd, equivalent to intake flow under stand-alone operations of the Carlsbad Desalination Plant producing product water at 50 mgd. Figure 14 gives the complementary velocity field in the West Basin for maximum ebb tide flow during spring tides. The existing EPS intake structure is located at this straight section of bank. Seawater entering the existing EPS intake structure passes through metal trash racks, with vertical bars that are spaced about 8.9 cm (3½ in) apart. Behind the trash racks vertical traveling water screens are positioned to prevent fish and debris from entering the sea water circulation system and potentially clogging the condensers. The traveling screens are to be upgraded by eight Bilfinger Water Technologies (BWT) center-flow traveling water screens with 1.0-mm mesh with through screen velocity of 0.5 ft/s. The screens would be modified with fish protection features, including: fish lifting buckets on each screen basket, low pressure spraywash, and fish return system. Once organisms are removed from the BWT center-flow screens, they must be safely returned back to the Agua Hedionda Lagoon. In this regard, the important flow feature shown in both Figures 13 and 14 is a stagnation region delineated by the dark blue area north east of the existing intake structure. The fish return discharges from the BWT screens will be reintroduced into this quiescent area in the southeast corner of the lagoon thereby minimizing the potential for recirculation of returned organisms into the intake flow.

6) Conclusions:

This technical note details tidal hydraulic simulations of the flow field in Agua Hedionda Lagoon for the tidal conditions and flow augmentation anticipated for the long term stand-alone Carlsbad Desalination Project. These simulations allow us to map out the water circulation throughout the lagoon with special attention placed on the West Basin and the tidal inlet channel. These simulations reveal a quiescent area in the southeast corner of the West Basin of the lagoon where fish can be returned to the lagoon after recovery by up-graded fish screens without significant risk for recirculation of returned organisms into the intake flow.

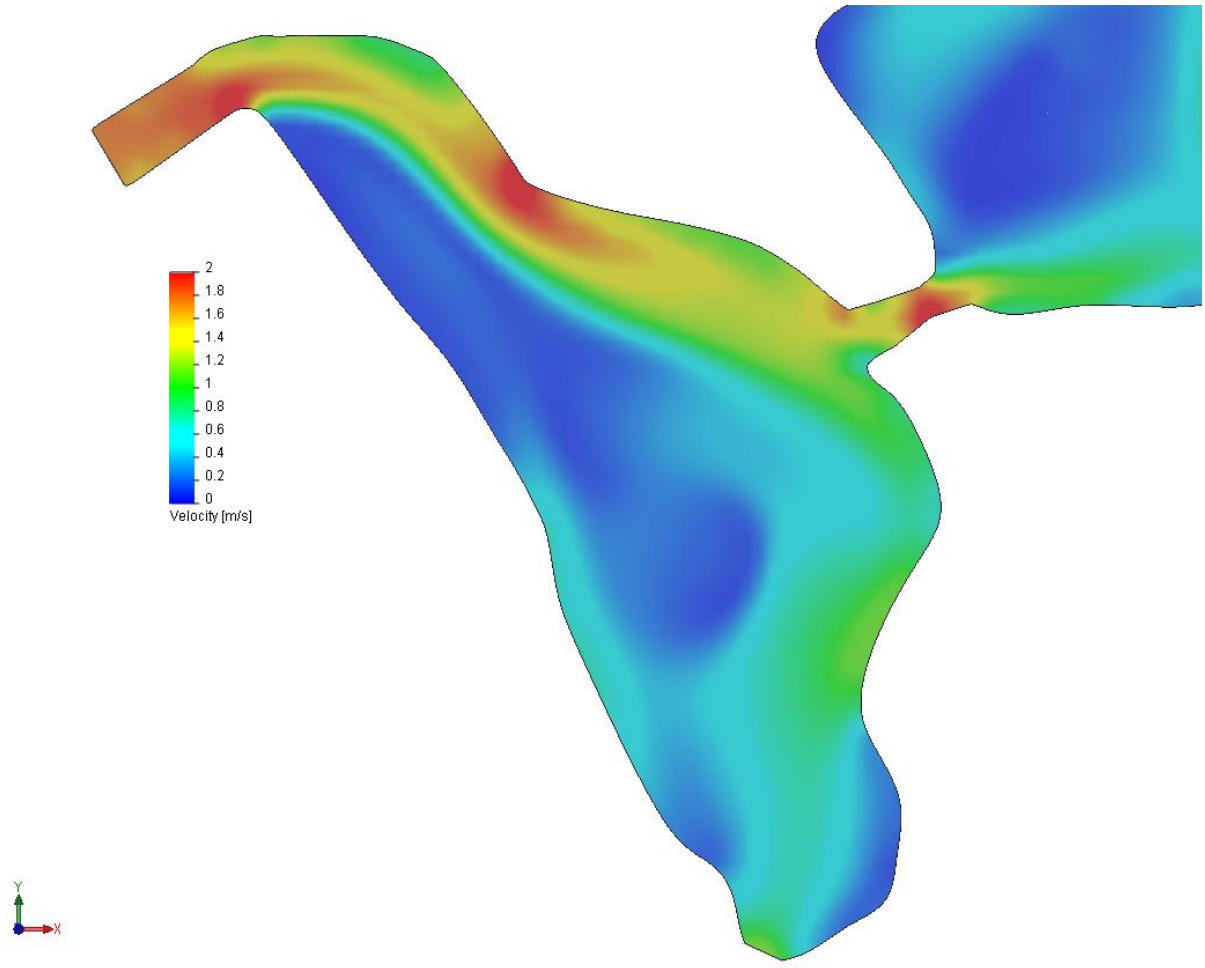

Figure 13: Velocity contour for maximum flood tide flow during spring tide with intake flow rate at Q = 304 mgd.

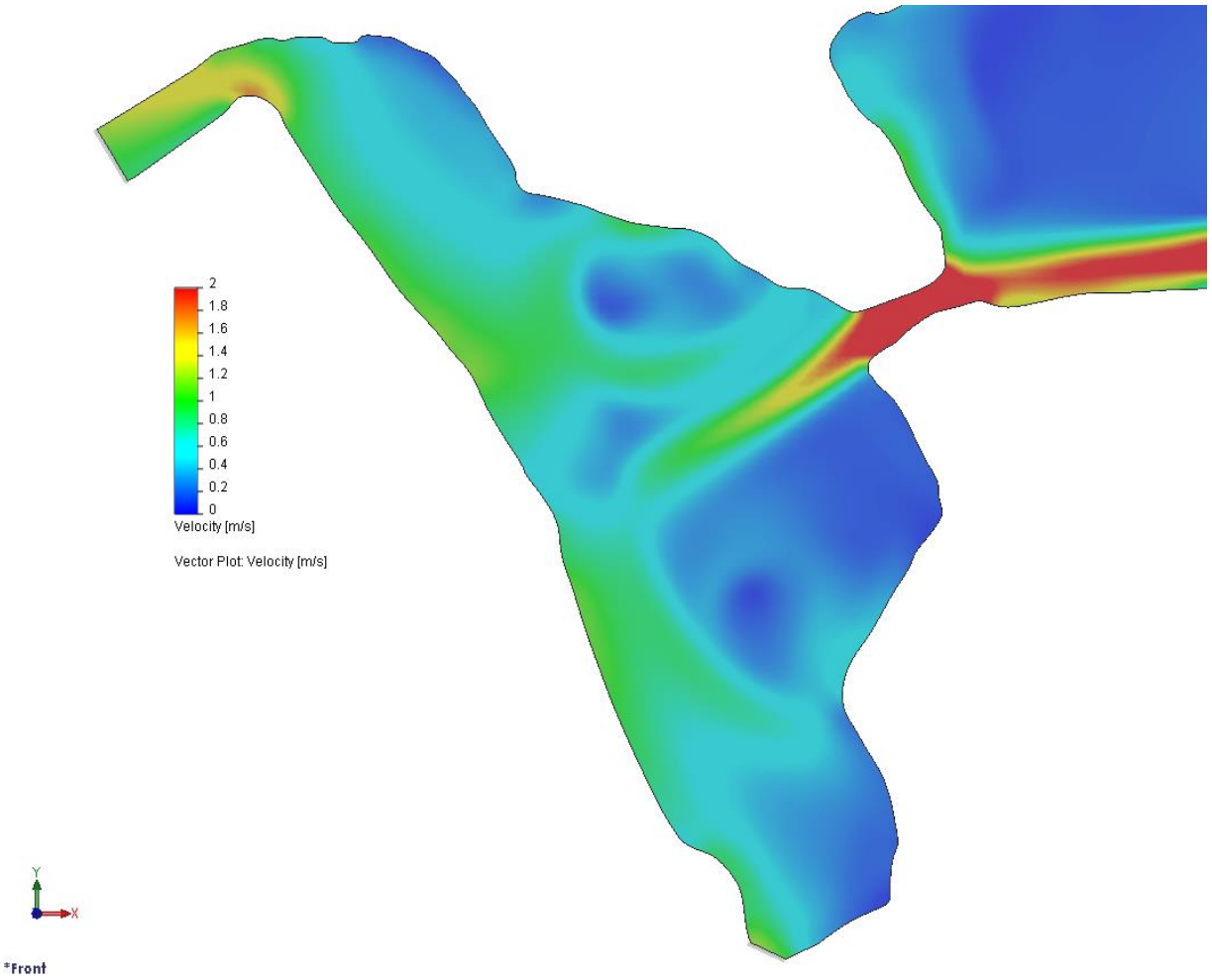

Figure 14: Velocity contour for maximum ebb tide flow during spring tide with intake flow rate at Q = 304 mgd.

7) Bibliography:

Batchelor, G. K., 1970 *An Introduction to Fluid Mechanics*, Cambridge University Press, 615 pp.

EIR, 2005 "Precise Development Plan and Desalination Plant," EIR 03-05-Sch #2004041081, prepared for City of Carlsbad by Dudek and Associates, December, 2005.

Elwany, M. H. S., A. L. Lindquist, R. E. Flick, W. C. O'Reilly, J. Reitzel and W. A. Boyd, 1999, "Study of Sediment Transport Conditions in the Vicinity of Agua Hedionda Lagoon," submitted to California Coastal Commission, San Diego Gas & Electric, City of Carlsbad.

Elwany, M. H. S., R. E. Flick, M. White, and K. Goodell, 2005, "Agua Hedionda Lagoon Hydrodynamic Studies," prepared for Tenera Environmental, 39 pp. + appens.

Jenkins, S. A**.** & J. Wasyl, 1990, "Resuspension of estuarial sediments by tethered wings," *Jour. Coastal Res.,* v. 6, n. 4, p. 961–980.

Jenkins, S. A. and J. Wasyl, 2005, "Hydrodynamic Modeling of Dispersion and Dilution of Concentrated Seawater Produced by the Ocean Desalination Project at the Encina Power Plant, Carlsbad, CA, Part II: Saline Anomalies due to Theoretical Extreme Case Hydraulic Scenarios*,"* submitted to Poseidon Resources, 97pp.

Jenkins, S. A. and J. Wasyl, 2005, "Coastal evolution model," Scripps Institution of Oceanography Tech Report No. 58, 179 pp + appendices. http://repositories.cdlib.org/sio/techreport/58/

Jenkins, S. A. and D. L. Inman, 2006, "Thermodynamic solutions for equilibrium beach profiles", *Jour. Geophys. Res.*, v.3, C02003, doi:10.1029, 21pp.

Jenkins, S. A., J. Paduan, P. Roberts, D. Schlenk, and J. Weis, 2012, "Management of Brine Discharges to Coastal Waters; Recommendations of a Science Advisory Panel", submitted at the request of the California Water Resources Control Board, 56 pp. + App.

Jenkins, S. A., 2013, "Technical Memorandum: Shoreline Evolution Analysis of Impacts Related to Removal of the South Beach Groin at Encina Power Station, Carlsbad," submitted to NRG Energy, 90 pp.

Jessopp, M.J., 2007, "The quick and the dead: larval mortality due to turbulent tidal transport", *J.Mar. Biol. Ass*., UK, vol. 87., pp 675-680.

Lafferty, K. D., R. O. Swenson and C. C. Swift, 1996, "Threatened fishes of the world: *Eucyclogobius newberryi* Girard, 1857 (Gobiidae). *Environmental Biology of Fishes*, v. 46, p. 254.

Morgan, R. P., R. E., Ulanowicz, V. J., Rasin, L.A., and G. B. Gray, 1974, "Effects of shear on eggs and larvae of the striped bass, Norene saxatilis, and the white perch," *Transactions of the American Fisheries Society*,45:2, 20-31.

Neitzel, D. A., M. C. Richmond, D. D. Dauble, R. P.Mueller, R. A., Moursund, C. S. Abernethy, G. R., Guensch, and G. F. Cada. 2000. "Laboratory studies on the effects of shear on fish". U. S. Department of Energy, Idaho Operations Office, DOE/ID-10822, Idaho Falls, Idaho.

Neitzel, D.A. , D. D. Dauble , G. F. ada , M. C. Richmond , G. R. Guensch , R. P. Mueller , C. S. Abernethy & Brett Amidan (2004) "Survival Estimates for Juvenile Fish Subjected to a Laboratory-Generated Shear Environment," Transactions of the American Fisheries Society, 133:2, 447-454, DOI: 10.1577/02-021

O'Connor, J. M. 1 and G. V. Poje. 1979. Power plant entrainment simulation utilizing a condenser tube simulator. NUREG/CR-0894. U.S. Nuclear Regulatory Commission, Washington, D.C. 103 pp.

SWRCB, 2014, "DESALINATION FACILITY INTAKES, BRINE DISCHARGES, AND THE INCORPORATION OF OTHER NONSUBSTANTIVE CHANGES, Draft Staff Report Including the Draft Substitute Environmental Documentation Amendment to the Water Quality Control Plan For Ocean Waters of California, 206 pp.

Tenera, 2008, **"**Cabrillo Power I LLC, Encina Power Station 316(b) Cooling Water Intake Impingement Mortality and Entrainment Characterization Study: Effects on the Biological Resources of Agua Hedionda Lagoon and the Nearshore Ocean Environments" submitted to NRG Energy, 220 pp

Ulanowicz, Robert E. (1976) "The mechanical effects of water flow on fish eggs and larvae". In: Saila, S.B. (ed.) Fisheries and energy production: a Symposium. Lexington, MA, D.C. Heath, pp. 77-87.

USACE, 1993, "Existing State of San Diego County Coast," US Army Corps of Engineers, Los Angeles District, Tech Rpt 93-1, 335 pp.

Weston Solutions, (2013), “High-Salinity Sensitivity Study: Short- and Long-Term Exposure Assessments”, submitted to West Basin Municipal Water District, 571 pp. http://www.waterboards.ca.gov/water_issues/programs/ocean/desalination/dos/sal study4wbmd.

Wygnanski, I. and H. E. Fiedler (1969). "Some Measurements in the Self-Preserving Jet."Journal of Fluid Mechanics 38(3): 577-612

APPENDIX-I: Tidal Hydraulics Model Physics:

The tidal hydraulics are treated herein as a vertically well-mixed, two-dimensional, homogeneous flow because of a number of factors, including: the shallow depths in all three basins of Agua Hedionda Lagoon; the episodic and usually infrequent river flow events; and the enormous complexity of attempting to model a continuously stratified, brackish system. Salinity measurements from the Entrainment/Impingement Study by Tenera (2007) suggest that this is not an unrealistic approximation. These salinity measurements indicate fairly uniform seawater salinities exist in the estuary most of the time, with relatively brief periods of fresh water dominance when high river flow rates prevent saline intrusion, e.g., the February 1995 flood series. Consequently, the Agua Hedionda Lagoon is a tidally dominated system throughout most any given long-term period of record.

A finite element approach was adapted in preference to more common finite difference shallow water tidal models, e.g., Leendertse (1970), Abbott et al (1973), etc. Finite difference models employ rectangular grids which would be difficult to adapt to the complex. It is believed that large errors would accumulate from attempting to approximate the irregular boundaries of the Agua Hedionda Lagoon system with orthogonal segments. On the other hand, finite element methods allow the computational problem to be contained within a domain bounded by a continuous contour surface, such as the S_f contours stored within the ***bathym*** file.

A finite element tidal hydraulics model, **TIDE_FEM**, [Inman and Jenkins, 1996] was employed to evaluate the tidal hydraulics of the existing conditions. **TIDE_FEM** was built from some well-studied and proven computational methods and numerical architecture that have done well in predicting shallow water tidal propagation in Massachusetts Bay [Connor and Wang, 1974] and estuaries in Rhode Island, [Wang, 1975], and have been reviewed in basic text books [Weiyan, 1992] and symposia on the subject, e.g., Gallagher (1981).

TIDE_FEM employs a variant of the vertically integrated equations for shallow water tidal propagation after Connor and Wang (1975). These are based upon the Boussinesq approximations with Chezy friction and Manning's roughness. The finite element discretization is based upon the commonly used ***Galerkin weighted residual method*** to specify integral functionals that are minimized in each finite element domain using a variational scheme, see Gallagher (1981). Time integration is based upon the simple ***trapezoidal rule*** [Gallagher, 1981]. The computational architecture of **TIDE_FEM** is adapted from Wang (1975), whereby a transformation from a **global** coordinate system to a **natural** coordinate system based on the unit triangle is used to reduce the weighted residuals to a set of order-one ordinary differential equations with constant coefficients. These coefficients (***influence coefficients***) are posed in terms of a ***shape function*** derived from the natural coordinates of each nodal point. The resulting systems of equations are assembled and coded as banded matrices and subsequently solved by ***Cholesky's method***, see Oden and Oliveira (1973 and Boas (1966).

We adapt the California coordinates as our **global** coordinate system (x, y) to which the nodes are referenced, with **x** (easting) and **y** (northing). The vertical coordinate **z** is fixed at 0.0 ft NGVD and is positive upward. The local depth relative to 0.0 ft NGVD is **h** and the mean surface elevation about 0.0 ft NGVD is **η**. The total depth of water at any node is **H = h + η**. The vertically averaged xy-components of velocity are $(\bar{u}, \bar{v})$. The continuity and momentum equations may be written from Connor and Wang, (1974), as:

$$\frac{\partial}{\partial t}\rho H + \frac{\partial}{\partial x}q_x + \frac{\partial}{\partial y}q_y = 0$$

$$\frac{\partial}{\partial t}q_x + \frac{\partial}{\partial x}\bar{u}q_x + \frac{\partial}{\partial y}\bar{u}q_y = B_x + \frac{\partial}{\partial x}\left(\quad_{xx} \square F_p \right) + \frac{\partial}{\partial x}F_{yx} \qquad (1)$$

$$\frac{\partial}{\partial t}q_y + \frac{\partial}{\partial x}\bar{v}q_x + \frac{\partial}{\partial y}\bar{v}q_y = B_y + \frac{\partial}{\partial y}\left(F_{yy} \square F_p\right) + \frac{\partial}{\partial x}F_{xy}$$

Here $\mathbf{q_x}$, $\mathbf{q_y}$ are mass flux components

$$q_x = \rho \int_{-h}^{\eta} \bar{u}\, dz \qquad (2)$$

$$q_y = \rho \int_{-h}^{\eta} \bar{v}\, dz \qquad (3)$$

and $\mathbf{q_I}$ is the mass flux through the ocean inlet due to water surface elevation changes in the estuary:

$$q_I = \rho \frac{\partial}{\partial t}\left(\frac{\partial s}{\partial \eta} \right) \qquad (4)$$

$\mathbf{F_p}$ is the pressure force resultant and $\mathbf{F_{xx}}$, $\mathbf{F_{xy}}$, $\mathbf{F_{yy}}$ are "equivalent" internal stress resultants due to turbulent and dispersive momentum fluxes

$$
\begin{aligned}
F_p &= \int_{-h}^{\eta} p\,dz = \frac{\rho g H^2}{2} \\
F_{xx} &= 2\varepsilon \frac{\partial}{\partial x} q_x \\
F_{yy} &= 2\varepsilon \frac{\partial}{\partial y} q_y \\
F_{yx} &= F_{xy} = \varepsilon \left(\frac{\partial}{\partial y} q_y + \frac{\partial}{\partial x} q_x \right)
\end{aligned}
\tag{5}
$$

and ε is the eddy viscosity. $\mathbf{B_x}$ and $\mathbf{B_y}$ are the bottom stress components

$$
\begin{aligned}
B_x &= \tau_x + \rho g H \frac{\partial h}{\partial x} \\
B_y &= \tau_y + \rho g H \frac{\partial h}{\partial y}
\end{aligned}
\tag{6}
$$

In Equation (6), $\boldsymbol{\tau_x}$ and $\boldsymbol{\tau_y}$ are the bottom shear stress components that are quasi-linearized by Chezy-based friction using Manning's roughness factor, $\mathbf{n_o}$:

$$
\begin{aligned}
\tau_x &= -\frac{g}{\rho H^2 C_z^{\,2}} q_x \left(q_x^{\,2} + q_y^{\,2} \right)^{1/2} \\
\tau_y &= -\frac{g}{\rho H^2 C_z^{\,2}} q_y \left(q^{x\,2} + q^{y}{}_{2} \right)^{1/2}
\end{aligned}
\tag{7}
$$

where $\mathbf{C_z}$ is the Chezy coefficient calculated as:

$$
C_z = \frac{1.49}{n_0} H^{1/6} \tag{8}
$$

Boundary conditions are imposed at the locus of possible land/water boundaries, $\mathbf{S_f}$ in the ***bathym*** file and at the ocean inlet, $\mathbf{S_o}$. Flux quantities normal to these contours are denoted with "n" subscripts and tangential fluxes are given "s" subscripts. At any point along a boundary contour, the normal and tangential mass fluxes are:

$$
\begin{aligned}
q_n &= \int_{-h}^{\eta} \rho u_n dz = \alpha_{nx} q_x + \alpha_{ny} q_y \\
q_s &= \int_{-h}^{\eta} \rho u_s dz = -\alpha_{nx} q_x + \alpha_{ny} q_y \\
\alpha_{nx} &= \cos(n, x) \\
\alpha_{ny} &= \cos(n, y)
\end{aligned}
\tag{9}
$$

Components of momentum fluxes across a boundary are equivalent to internal force resultants according to:

$$
\begin{aligned}
F_{nx} &= \alpha_{nx}(F_{xx} - F_p) + \alpha_{ny} F_{yx} \\
F_{ny} &= \alpha_{ny}(F_{yy} - F_p) + \alpha_{nx} F_{xy}
\end{aligned}
\tag{10}
$$

On land boundary contours, the flux components are prescribed

$$q_n = q_s = 0 \qquad \text{on land} \tag{11}$$

On the ocean boundary, the normal boundary forces (due to sea surface elevation) are continuous with ocean values, and the mass exchange is limited by the storage capacity of the estuary. Hence

$$F_{nm} = \bar{F}_{nm} \quad \text{and} \quad q_{nm} = q_I \qquad \text{at inlet} \tag{12}$$

In the problem at hand $\bar{F}_{nn}$ is prescribed at the inlet by the ocean tidal elevation, η_0 , and the inlet sill depth, $\mathbf{h_o}$ according to

$$\bar{F}_{nm} = \frac{\rho g}{2}(\eta_0 + h_0)^2 \qquad \text{on } S_0 \tag{13}$$

Ocean ***tidal forcing functions*** η_0 were developed in Section 3. The ocean boundary condition as specified by Equation (12) places a dynamic boundary condition on the momentum equations and a kinematic boundary condition on the continuity equation that is constrained by the storage rating curve. Solutions are possible by specifying only the dynamic boundary condition, but then mass exchanges are controlled by the wetting and drying of individual grid cells with associated discretization and interpolation errors which threaten mass conservation. The technique of over specifying the ocean boundary condition with both a dynamic and kinematic condition is discussed in the book by Weiyan (1992).

The governing equations and the boundary conditions are cast as a set of integral functionals in a variational scheme, [Boas, 1966]. Within the domain of each element of the mesh, $\mathbf{A_i}$ the unknown solution to the governing equations is simulated by a set of ***trial functions*** $(\hat{H}, \hat{q})$ having adjustable coefficients. The trial functions are substituted into the

governing equations to form ***residuals,*** $\mathbf{(R_H, R_q)}$. The residuals are modified by ***weighting functions,*** $\mathbf{(\Delta H, \Delta q)}$. The coefficients of the trial functions are adjusted until the weighted residuals vanish. The solution condition on the weighted residuals then becomes:

$$\iint_{A_i} R_H \Delta H dA = 0$$

$$\iint_{A_i} R_q \Delta q dA = 0$$

By the Galerkin method of weighted residuals, [Finlaysen, 1972], the weighting functions are set equal to nodal ***shape functions***, **<N>**, or:

$$\Delta H \sim N_i$$

$$\Delta q \sim N_j$$

The shape function, <N>, is a polynomial of degree which must be at least equivalent to the order of the highest derivative in the governing equations. The shape function also provides the mechanism to discretized the governing equations. The shape function polynomial is specified in terms of ***global (California)*** coordinates (A-1a) for the first nodal point, $\mathbf{N_1}$ of a generalized

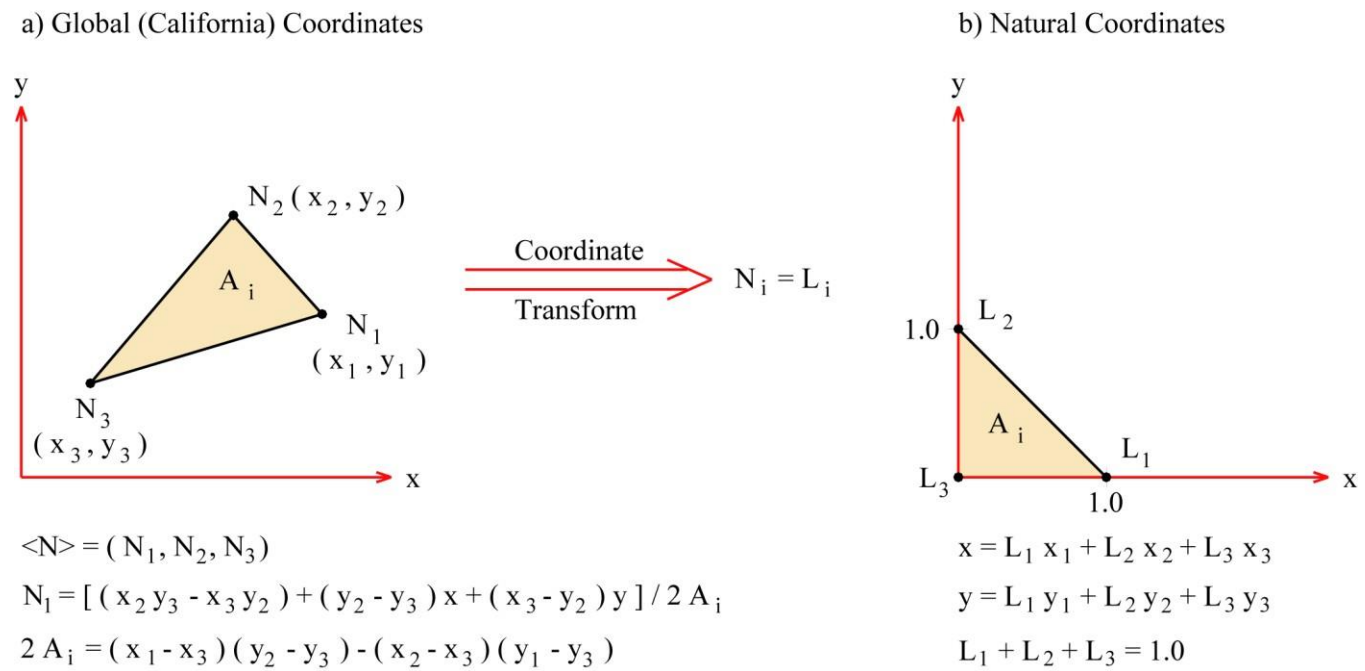

Figure A-1: Shape function polynomial and transform to natural coordinates for a generalized 3-node triangular element; (a) 3-node element in California coordinates; (b) 3-node element in natural coordinates.

3-node triangular element of area $\mathbf{A_i}$,. Wang (1975) obtained significant numerical efficiency in computing the weighted residuals when the shape functions of each nodal point, $\mathbf{N_i}$, are transformed to a system of ***natural*** coordinates based upon the unit triangle, giving $\mathbf{N_i} \rightarrow \mathbf{L_i}$, see Figure A-1b. The shape functions also permit semi-discretization of the governing equations when the trial functions are posed in the form:

$$\hat{H}(x,y,t) = \sum_i H_i(t) N_i(x,y)$$
$$\hat{q}(x,y,t) = \sum_j q_j(t) N_j(x,y) \qquad (14)$$

Discretization using the weighting and trial functions expressed in terms of the nodal shape functions allows the ***distribution*** of dependent variables over each element to be obtained from the values of the independent variables at discrete nodal points. However, the shape function at any given nodal point, say $\mathbf{N_1}$, is a function of the independent variables of the two other nodal points which make up that particular 3-node triangular element. Consequently, the computations of the weighted residuals leads to a series of influence coefficient matrices defined

$$a_{ij} = \frac{1}{A_i} \iint N_i N_j \, dA$$
$$s_{ij} = \frac{1}{A_i} \iint N_i \frac{\partial N_j}{\partial x} dA$$
$$t_{ij} = \frac{1}{A_i} \iint N_i \frac{\partial N_j}{\partial y} dA \qquad (15)$$

$$g_{ijk} = \frac{1}{A_i} \iint N_i N_j \frac{\partial N_k}{\partial x} dA$$
$$h_{ijk} = \frac{1}{A_i} \iint N_i N_j \frac{\partial N_k}{\partial y} dA$$

The influence coefficient matrices given by equation (15) are evaluated in both global and natural coordinates. Once the influence coefficients have been calculated for each 3-node element, the weighted residuals reduce to a set of order-one ordinary differential with constant coefficients. The continuity equation becomes:

$$\sum_i \left(a_{ij} \frac{dH_i}{dt} \right) = -\sum_k \sum \left[g_{ijk} \left(H_i q_{xk} + H_k q_{xi} \right) + h_{ijk} \left(H_i q_{yk} + H_k q_{yi} \right) \right]$$

$$\sum_j \left(a_{ij} \frac{dq_{xj}}{dt} \right) = -\sum_k \sum \left[g_{ijk} \left(q_{xk} q_{xj} \right) + h_{ijk} \left(q_{yj} q_{xk} \right) \right] + N_i \sum_j N_j S_{fj} + g \sum_i s_{ij} H_i \qquad (16)$$

$$\sum_j \left(a_{ij} \frac{dq_{yj}}{dt} \right) = -\sum_k \sum \left[g_{ijk} \left(q_{xj} q_{yk} \right) + h_{ijk} \left(q_{yj} q_{xk} \right) \right] + N_i \sum_j N_j S_{fj} + g \sum_i t_{ij} H_i$$

Equations (16) are essentially simple oscillator equations forced by the collection of algebraic terms appearing on the right hand side; and are therefore easily integrated over time. The time integration scheme used over each time step of the tidal forcing function is based upon the ***trapezoidal rule***, see Gallagher 1981) or Conte and deBoor (1972). This scheme was chosen because it is known to be unconditionally stable, and in tidal propagation problems has not been known to introduce spurious phase differences or damping. It replaces time derivatives between two successive times, $\Delta t = t_{n+1} - t_n$, with a truncated Taylor series. For the water depth it would take on the form:

$$\frac{dH}{dt} = \eta(t)$$

$$H_{n+1} - H_n = \frac{\Delta t}{2} \left(\eta_{n+1} + \eta_n \right) + E \Delta t \qquad (17)$$

$$E = \frac{1}{12} (\Delta t)^2 \left| \frac{d\ \eta}{dt^2} \right|$$

To solve equation (17), iteration is required involving successive forward and backward substitutions.

The influence and friction slope coefficient matrices together with the trapezoidal rule reduce equations to a system of algebraic equations [Grotkop, 1973] which are solved by Cholesky's method per a numerical coding scheme by Wang (1975). For more details, refer to the TIDE_FEM code in Appendix-I of Jenkins and Wasyl (1996), and Gallagher (1981) or Oden and Oliveira (1973).